ORIGINAL RESEARCH

Optical Time-Resolved Diagnostics of Laser-Produced Plasmas

D. Batani[1,7] · J. Santos[1] · P. Forestier-Colleoni[1] · D. Mancelli[1,8] · M. Ehret[1] · J. Trela[1] · A. Morace[2] ·
K. Jakubowska[3] · L. Antonelli[4] · D. del Sorbo[5] · M. Manclossi[6] · M. Veltcheva[6]

Abstract

The paper presents the general challenges of diagnostics for laser-produced plasmas related to their small dimensions and short duration but also to the presence of very strong temperature and density gradient in the plasma. In particular, we focus on more detailed examples related to optical diagnostics for the undercritical region of the plasma: shadowgraphy, schlieren, interferometry, polarimetry.

Keywords Laser-produced plasmas · Inertial confinement fusion · Optical diagnostics

Introduction

Laser produced plasmas are relevant for basic physics and for applications, as well as inertial confinement fusion. Because of this large interest, many diagnostics have been developed and are used to study the physical processes taking place during laser–plasma interaction.

Apart from the general challenges related to plasma diagnostic, the diagnostics of laser-produced plasmas pose some specific challenges. First of all, laser produced plasmas are small and have a short duration. Typically, the size is comparable to the laser spot dimension (μm to mm) and the time life is comparable to the laser pulse duration (after the end of the laser pulse the plasma rapidly cools down and vanishes). Hence diagnostics need to have high spatial and temporal resolution.

But the main challenge arises from the fact that the temperature and density of laser-produced plasmas span over several orders of magnitude and are characterized by the presence of very distinct plasma "regions" all simultaneously present.

1. First the "undercritical region" (or plasma corona) is defined by having a density smaller than the laser critical density, in practical units:

$$n_{cr}\,(\mathrm{cm}^{-3}) = 1.1 \times 10^{21}/\lambda^2\,(\mu m) \qquad (1)$$

In this region, the density decreases (due to plasma expansion) going away from the target surface. Also, this region is directly heated by the laser, which can propagate up to n_{cr}, and therefore it reaches high temperatures: a few 100 eV up to a few keV.

2. Then we have the "conduction region", or overcritical region, where the laser cannot propagate. Here heat is transported inwards by electrons or by XUV—soft X-ray radiation generated in the corona. From the value reached in the corona, the temperature drops down to a few eV. The electron density increases from the n_{cr} value up to the electronic density of solid matter.

3. Finally we have the "shocked material". Plasma expansion produces, due to momentum conservation, a shock travelling inward and compressing the target.

✉ D. Batani
dimitri.batani@u-bordeaux.fr

1   CEA, CNRS, CELIA (Centre Laser Intense at Applications), UMR 5107, University Bordeaux, 33405 Talence, France

2   ILE, Institute of Laser Engineering, University of Osaka, Osaka, Japan

3   IPPLM, Warsaw, Poland

4   University of York, York, UK

5   High Energy Density Science Division, SLAC National Accelerator Laboratory, Menlo Park, CA 94025, USA

6   LOA, ENSTA, Palaiseau, France

7   Department of Plasma Physics, National Research Nuclear University MEPhI, Moscow, Russia

8   Donostia International Physics Center (DIPC), Donostia-San Sebastian, Basque, Spain

The generated pressure can be as high as a few MBars and compression heats the material up to a few eV. Ahead of the shocked region we have the still unperturbed solid.

Due to the differences of several orders of magnitude in density and temperature among the different regions, different diagnostics are needed.

For instance, the plasma corona, where a probe laser beam can propagate, can be characterized by optical diagnostics: interferometry [1], shadowgraphy [2, 3], Faraday rotation [4], etc. Also, this region is very hot and hence emits X-rays. Therefore, one can use X-ray spectroscopy [5–9]. Optical spectroscopy can be useful to characterize parametric instabilities taking place in laser–plasma interaction [10–12]. And finally, one can use particle detection (charge collectors, Faraday's cups, etc.) [13].

The overcritical region is the main source of soft X-rays and XUV radiation because, even if the temperature is on average lower than in the corona, the density is much larger and then there are more collisions and photon emission. Hence one can sue emission X-ray spectroscopy and absorption X-ray spectroscopy [14, 15]. However, unlike the plasma corona, this region is optically thick which implies that there is a strong re-absorption of emitted photons and hence opacity effects must be taken into account. In principle one can use also XUV interferometry (for instance with XUV laser sources) but in reality, this is quite challenging [16].

The shocked region is particularly difficult to be probed. Due to its low temperature, there is no strong emission of radiation and this is concentrated at long wavelength, also this region is very opaque due to its large density. One can use X-ray radiography with hard X-rays emitted from a secondary laser-produced source [17], or proton radiography [18]. With sufficiently thin targets, it is also possible to use optical diagnostics: when the shock breaks out on the target "rear side", matter is heated and intense thermal radiation is emitted which can be recorder and time resolved, for instance, suing a streak camera [19–21].

To complete the panorama, one should cite all diagnostics which are typical of laser-driven inertial fusion experiments: neutron measurements [22], neutron spectroscopy [23], neutron imaging [24].

Of course, it is not possible to deal with all such different diagnostics in a single paper. Therefore, we will just concentrate on a few examples and, in particular, we will focus on optical diagnostics for the undercritical region of the plasma: shadowgraphy, schlieren, interferometry, polarimetry, where the presence of the plasma impacts the behavior of an electromagnetic (e.m.) wave of angular frequency ω.

Optical Shadowgraphy and Schlieren

Plasma of electronic density n_e (in the limit of low collisionality and when no external magnetic fields are present) has a refraction index n given by

$$n = \sqrt{1 - \frac{\omega_p^2}{\omega^2}} = \sqrt{1 - \frac{n_e}{n_{cr}}}$$

where ω is the frequency of the e.m wave (i.e. the laser in our case). For an undercritical plasma ($n_e < n_{cr}$) the refraction index is real and < 1, and for the case of much underdense plasmas ($n_e \ll n_{cr}$) it becomes

$$n \approx 1 - \frac{n_e}{2n_{cr}}$$

The gradients of density, which are always present and strong in laser-produced plasmas, then induce a gradient of refraction index $\nabla n \approx -\nabla n_e / 2n_{cr}$. According to Snell–Descartes law of refraction, such gradient induces a deviation of the light ray by an angle

$$\theta = \frac{1}{n_{cr}} \frac{\partial}{\partial y} \int n \, dl \tag{2}$$

This is at the base of the diagnostics techniques of shadowgraphy and schlieren (a complete analysis, see for instance [25] shows that shadowgraphy accounts for the second derivative of the density gradients in the plasma whereas schlieren photography records the first derivative of the plasma density gradients).

One usual approach is to use a laser probe beam (at intensity low enough so to not perturb the plasma by inducing additional ionization or heating), which "backlights" the plasma to be probed. In this case one can even use a slow detector to make the image of the plasma: in any case the detector will "see" the plasma only as long as the backlighting source is on. Hence the system will provide a "snapshot", i.e. a 2D plasma image obtained with a time resolution equal to the duration of the pulse of the probe laser beam. In the case of shadowgraphy for instance, we will see a "shadow" of the plasma because the refracted rays will be deviated away. This "normal" shadowgraphy (without a lens) differs from the so called "focused shadowgraphy" which we will describe in the following. Indeed in the cases of large density gradients, such as in laser generated plasmas, normal shadowgraphy may fail providing useful result for several reasons.

First, the image provided by the backlighter will superimpose to the image created on the detector by the plasma self-emission which of course is not time-resolved but lasts as long as the plasma is sufficiently hot to emits significantly in the range determined by the spectral

sensitivity of the detector. We therefore need to eliminate plasma self-emission.

Second, the plasma will very likely be almost completely transparent to the incoming laser light, therefore the detector will be illuminated everywhere with little contrast. We therefore need to use a diagnostic approach, which evidences the presence of density gradients in the plasma.

Third, even if the rays which go through the plasma are deviated according to Eq. 2, then these are "brought back" to the detector when we use an imaging system (which is usually the case). For instance, if we use a lens which makes an image of the plasma on the detector, it brings back the refracted light to the image point corresponding to the object point where the ray originates, i.e. it has been deviated. So, the imaging system "kills" the shadow.

Therefore, the complete experimental set-up of shadowgraphy includes a spatial filter in the focal plane of the imaging lens (see Fig. 1). This diaphragm will cut all the rays, which have been strongly refracted and will let the un-deviated rays to go through. These are typically the rays, which go "around" the plasma (as shown again in Fig. 1) and which therefore are normally focused in the lens focal point. The result will be a "shadow" of the plasma: the plasma will look darker because most of the rays going though it are cut by the diaphragm. The recorded image is therefore called a "negative image" in opposition to the case of normal shadowgraphy where no lenses and no pin-hole are used. An alternative (up to a point depending on the optical system used and the density gradients of the plasma) is to "de-focus" the image by placing the lens not exactly at its focal position. This will enable a combination of the non-focused shadowgraphy with the focused shadowgraphy giving images suitable for analysis. Furthermore, by knowing the defocusing length, quantitative analysis can be performed giving absolute results for the plasma density. This is called quantitative shadowgraphy [26].

It is also possible to use the refraction fringes surrounding the accessible region of the plasma in order to calculate the density at the boundary of the corona plasma. This pattern is due to the refraction of the laser rays at the steep density gradient boundary of the plasma-vacuum interface [27, 28].

Normally strong gradients exist mainly at the edge of the plasma and thus shadowgraphy allows obtaining an image of the edges of the plasma. By changing the delay Δt between the beam creating the plasma and the probe beam, one can obtain a series of "frozen images" (i.e. 2D images integrated in time over the, short, duration of the probing laser beam) which allows reconstructing the plasma dynamics i.e. for instance measuring the plasma size at different times, thus allowing determining the expansion velocity of the plasma.

In this sense, optical shadowgraphy and schlieren are part of the techniques known as "pump and probe" diagnostics.

Figure 2 shows an example. Here a laser beam (a Nd:YAG with E $\approx$ 100 mJ, λ = 1.064 μm, $\tau \approx$ 10 ns) is focused on a solid target (an iron needle) in air. The probe beam is an unconverted fraction of the main beam (i.e. the probe is also infrared in this case) and is sent across the plasma with a variable delay. A hot and dense plasma is created at the surface of the target. Such plasma begins a rapid expansion compressing the air around it and generating a shock wave, which travels in air. The figure shows the evolution of the generated shock wave at three different times following irradiation [The use of a cylindrical needle as a target helps avoiding the problems related to possible small tilts of the target. In the case of a planar target, this must be perfectly parallel to the probe rays, otherwise it will mask some of them shadowing the part of the plasma closer to the surface, which is the denser one. Of course, this problem becomes bigger and bigger as the lateral dimension of the planar foil increases].

Figure 3 shows instead an image of plasma created by focusing a laser beam in air. In this case the plasma is elongated along the direction of propagation of the laser beam (the same laser of Fig. 2 is used here).

Fig. 1 In-principle scheme of optical shadowgraphy with the pin-hole placed in the focal point of the imaging lens
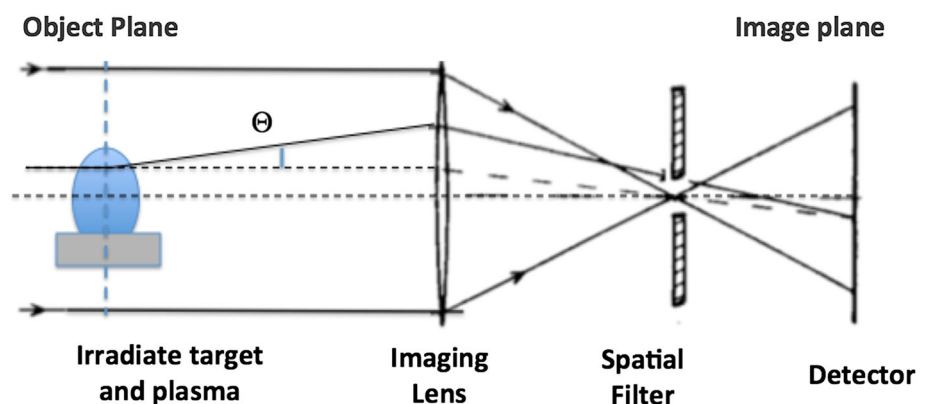
Fig. 2 Evolution of a laser-generated shock wave in air using schlieren. The 3 images correspond to delay t = 11.21 ns, 19.42 ns and 27.62 ns respectively. During this time the shock size (horizontal direction) increases from 177 to 192 μm, and finally 234 μm
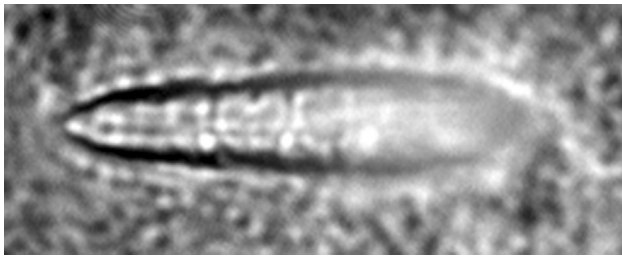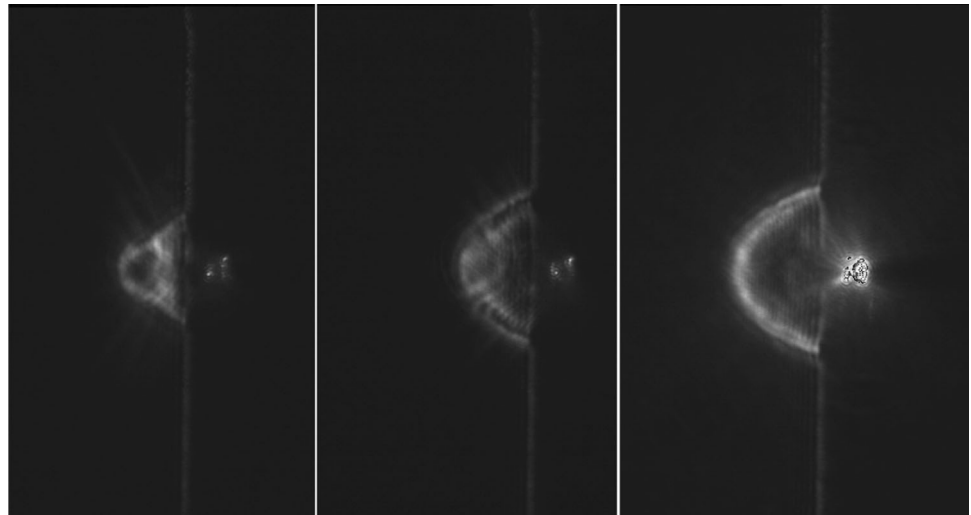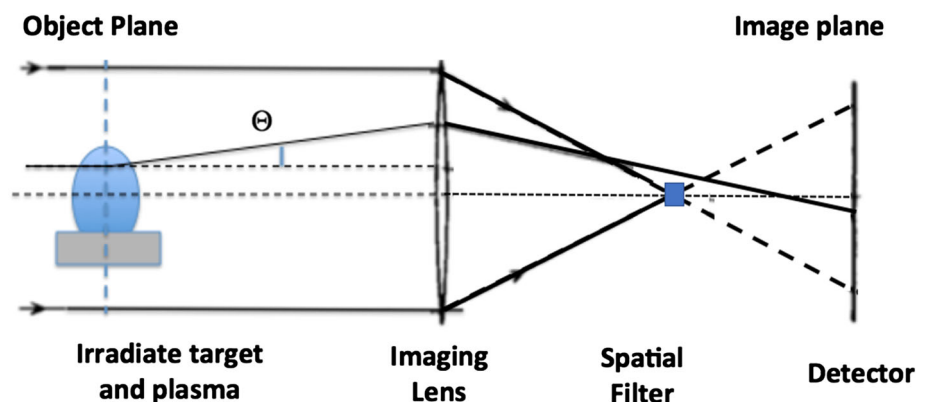

Fig. 3 Image of laser-induced plasma in air obtained using optical shadowgraphy. The probe beam crosses the plasma about 20 ns after the interaction of the pump beam has created the plasma. The size of the image is 200 × 460 μm

The drawback of shadowgraphy is the loss of spatial resolution. Indeed, the focal plane of the imaging lens realize the Fourier transform of the object to be imaged and the higher the spatial frequency, the bigger the distance from the focal point in the focal plane. Hence, placing a diaphragm in the focal plane means cutting the high-spatial frequencies (short spatial scales), which are essential in order to assure a detailed reconstruction of the image.

The schlieren technique is somewhat complementary to shadowgraphy. In this technique, we place an obstacle in the focal point of the imaging lens (see Fig. 4). Therefore, the refracted rays are allowed to go through while the un-refracted rays are cut. The strongly refracting zones are then materialized on the schlieren image by illuminated zones. Of course, schlieren allows maintain a good spatial resolution since it keeps the high spatial frequencies.

Figure 5 shows the comparison of shadowgraphy and schlieren in the case of the shock wave generated in air (as described about Fig. 2).

Finally, we close this paragraph by noticing that although shadowgraphy and schlieren are powerful diagnostic techniques, nevertheless they are mainly qualitative. As said before, one can attempt to do quantitative shadowgraphy or quantitative schlieren [29, 30] but indeed it is very difficult to retrieve the information on the density profile (this is not a surprise because indeed these diagnostics give information on the gradient of electron density or on its second derivative). An interesting development in this direction is however the development of the angular filter refractometry (AFR), which allows to characterize the

Fig. 4 In-principle scheme of schlieren with the obstacle placed in the focal point of the imaging lens

Fig. 5 Comparison of **a** conventional imaging, **b** shadowgraphy, and **c** schlieren techniques (same experimental configuration as in Fig. 2). The 3 images have been taken in identical conditions and with the same time delay
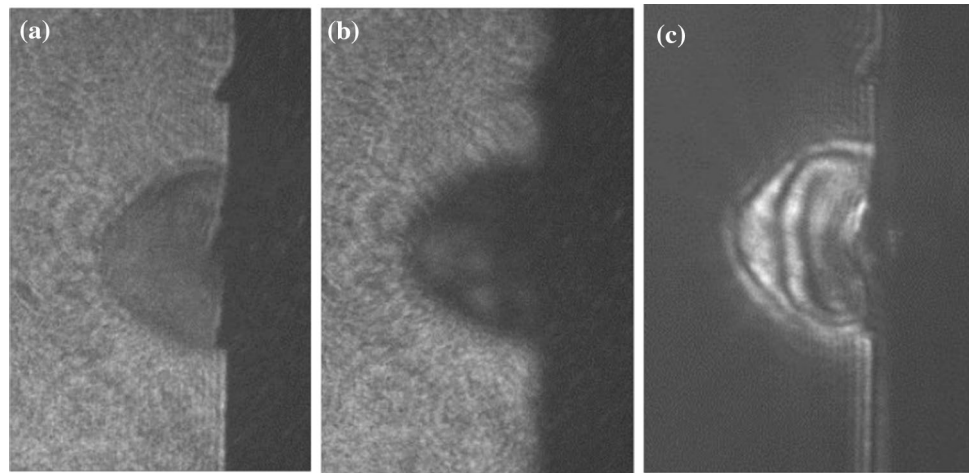
plasma density profile by producing a contour map of refraction angles [31]. This is accomplished by using angular filters (see Fig. 6) that block certain bands of refraction angles, producing shadows in the image plane. The plasma density is calculated from the measured refraction angles of a probe beam after passing through the plasma. The maximum measured density is limited by the f/# of the optical collection system as compared to the length of plasma in the direction of the probe and the magnitude of the transverse gradients (which determine the refraction angle through Eq. 2).

The AFR diagnostic uses an angular filter placed at the focus of the unrefracted probe beam (Fourier plane). The opaque regions of the angular filter block bands of refraction angles, resulting in shadows in the image plane. The diagnostic relies on the direct proportionality between the angle of refraction of a probe ray at the object plane and its radial location in the Fourier plane. This relation correlates the shadows produced by the angular filter with contours of constant refraction angle. For a single-lens imaging system and a collimated probe beam, it can be shown that a ray refracted at the object plane passes through the Fourier plane at a distance from the optical axis, r, which is equal to the focal length, f, of the collection lens times the refraction angle, Θ, regardless of its spatial origin in the object plane (assuming paraxial propagation). The direct proportionality of the spatial location of a ray to the amount of refraction allows for filtration of specific refraction angles in a deterministic manner. Depending on the value of the refraction angle, the probe rays will either be blocked by the opaque rings or transmitted between them, forming the light and dark bands in the image. By measuring the radial distance of each band, one can accurately calculate the refraction angles (again given by Eq. 2).

Chirped Optical Shadowgraphy

The technique of chirped pulse amplification (CPA) allows producing laser pulses with typical duration of hundreds ps to a few ns which are characterized by a chirp, i.e. a variation in time of the frequency. Normally this allows compressing the laser pulse in time inside a grating compressor, so to obtain short-duration very-high-intensity pulses. In the technique of chirped pulse shadowgraphy instead the beam is not compressed. The plasma to be probed is then illuminated with a chirped probe beam of relatively long duration. After the plasma, the beam is sent to an imaging spectrometer where the different wavelengths are dispersed in different direction. Since the different laser wavelengths arrive at different times on the plasma to be probed, we then have a univocal relation between time and wavelength.

In the imaging plane of the spectrometer we then get a 1D image resolved in time, as if we were operating with a

Fig. 6 Working scheme of the angular filter refractometry technique and example of filer used in the Focal plane (Fourier plane)

Imaging Lens　　**Angular Filter (Fourier Plane)**
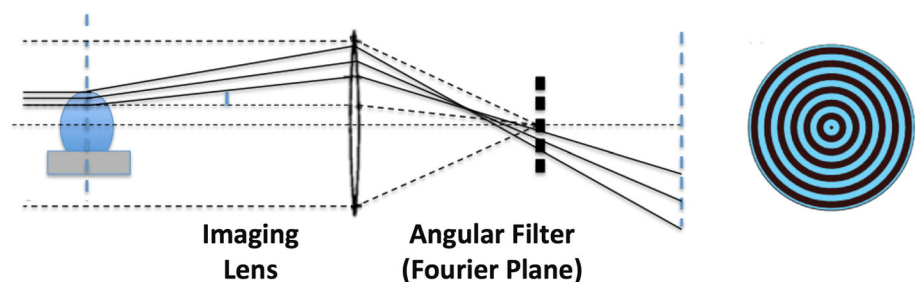
streak camera. However, the technique of chirped optical shadowgraphy allows getting a better time resolution.

This is a rather novel technique first introduced in [32]. In this experiment, optical shadowgraphy was to detect fast electron propagation in a gas medium. The region of the gas jet, which is ionized by the passage of fast electrons, creates a shadow in the recorded image. In [32] the chirped probe laser pulse was first compressed giving a 2D spatial resolution (classical shadowgraphy) and then, only partially compressed (i.e. still chirped) giving 1D time-resolved images (chirped shadowgraphy). In the first case, 2D snapshot images were obtained with the temporal resolution equal to the duration of the probe beam (< 350 fs). With this configuration, in relation to the propagation dynamics, several shots are needed with different delay between the main and probe beams. In the second case, only 1D images are obtained but the fast electron dynamics can be continuously followed in time over duration corresponding to the duration of the partially precompressed beam.

The scheme of the experimental set-up used in [32] is shown in Fig. 7. Fast electrons were created by a high-intensity laser on a thin foil (Ti) placed before a gas jet. Two gases (Ar and He) and different pressures were used.

Figure 8 shows shadowgrams obtained at different delays between the CPA beam and the probe. The cloud evolution can be followed and its average velocity between two different snapshots can be measured. However, as fast electron dynamics is inferred from several shots, the method is strongly affected by shot-to-shot fluctuations, greatly increasing error bars.

In chirped shadowgraphy the probe beam had longer pulse duration (τ = 19 ps) and was coupled to an imaging spectrometer. Here the gas medium (where the plasma is formed) is imaged on the entrance slit of the spectrometer, where the spectral axis through frequency dependence on time (chirp of the beam) corresponds to the temporal axis. The spatial resolution is obtained only in the direction parallel to the entrance slit. This diagnostic allows us to
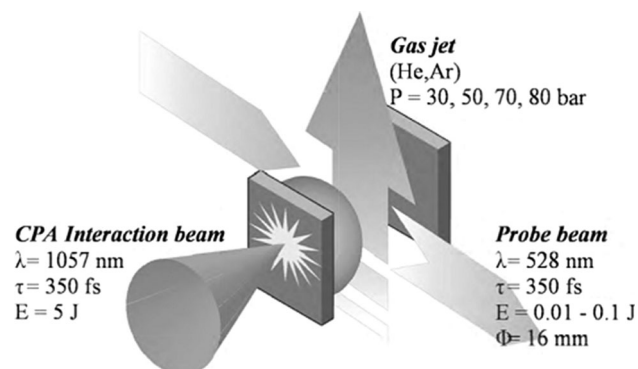
measure on a single laser shot the variation of the ionization front velocity with time resolving early times. Figure 9 shows chirped shadowgrams obtained with Ar at different pressures. The images in Fig. 9 clearly show the following:

1. The propagation velocity and the cloud penetration distance increase with gas pressure. This result agrees with those obtained with the classical shadowgraphy. The dimension of the cloud at the end of the image corresponds to the dimensions observed in the classical shadowgraphy images.

2. The propagation velocity slows down in time. Figure 9 (bottom) (Ar 100 bar) clearly shows first a fast speed $v_{AB} \sim 0.67c$, then a deceleration to a speed $v_{BC} \sim 0.16c$. In addition, we can note a cloud penetration over a distance of the order of the millimeter. The propagation velocity in Fig. 9 (top) (Ar 20 bar) is lower ($v_{AB} \sim 0.12c$) and the final propagation is much less important ($\sim$ 300 μm).

Figure 10 shows the temporal evolution of the cloud dimension for various gas pressures, obtained from the chirped shadowgraphy images, and clearly shows a deceleration occurring at the very first moments of the cloud propagation. This phase is very difficult to be observed with classical shadowgraphy since it would require taking many images at delays close to each other.

Interferometry

Interferometry is based on the fact that the plasma has a refractive index and hence the light rays crossing it experiences a phase shift. As before, for an undercritical plasma the refraction index n of a plasma is real and

$$n = \sqrt{1 - \frac{\omega_p^2}{\omega^2}} = \sqrt{1 - \frac{n_e}{n_c}} < 1$$

The plasma (of typical size L) must be placed within an interferometric system, for instance in one of the two arms of a Mach–Zender interferometer, as shown in Fig. 11.

Then the phase shift $\Delta\Phi$ induced by a homogeneous plasma will be

$$\Delta\Phi = (k_{plasma} - k_o)L = k_o(n-1)L = k_oL\left(\sqrt{1 - \frac{n_e}{n_c}} - 1\right)$$

which, in the case of much undercritical plasmas, reduces to

$$\Delta\Phi \approx \frac{k_oLn_e}{2n_c} \quad n_e \ll n_{cr}$$

We see therefore that interferometry can in this case directly provide the plasma density n_e. In the realistic case of non-homogeneous plasma, we have

Gas jet
(He,Ar)
P = 30, 50, 70, 80 bar

CPA Interaction beam
λ = 1057 nm
τ = 350 fs
E = 5 J

Probe beam
λ = 528 nm
τ = 350 fs
E = 0.01 - 0.1 J
Φ = 16 mm

Fig. 7 Schematic experimental set-up. The distance between the foils is 1.2 mm. Thickness is 20 μm (Ti) and 15 μm (Al) (from [32])

Fig. 8 Evolution of the electron cloud (He, 30 bar). From left: t = 10 ps, 16 ps, 50 ps. Bars correspond to 280, 540, and 1000 μm. The lower and upper dark parts in all images, respectively, represent the Ti and Al foils (from [33])
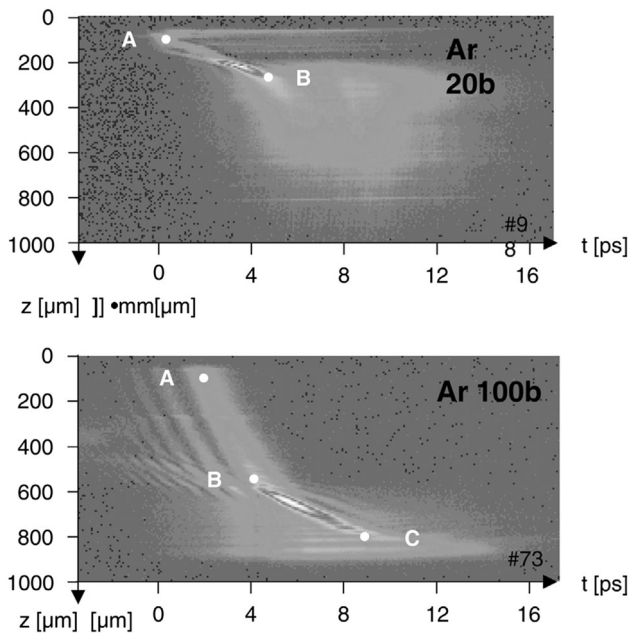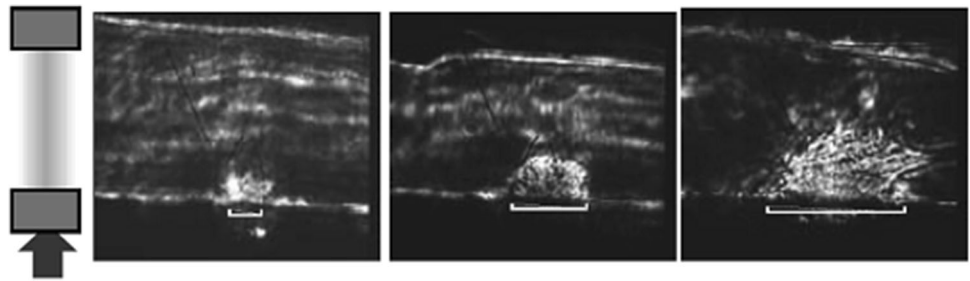

Fig. 9 Chirped shadowgraphy images obtained with a target of Al 15 μm and with a jet of argon to 20 bar (top) and to 100 bar (bottom). The laser intensity is 2×10^{19} W/cm². Time axis is the horizontal one and point A roughly represents the interaction time

Fig. 11 Mach–Zender interferometric set-up used to measure the plasma refraction index. The lens L_f images the plasma on the detector D

$$\Delta\Phi \approx \frac{k_0}{2n_{cr}} \int n_e \, dl \qquad (n_e \ll n_{cr})$$

which means that interferometry measures the total electronic areal density along the line of sight. Defining the average electronic density as

Fig. 10 Cloud size (top) and deduced velocity (bottom) versus time. Ar pressures are 10 bar (full circles), Ar 20 bar (empty circles), Ar 50 bar (full diamonds), Ar 100 bar (empty diamonds)
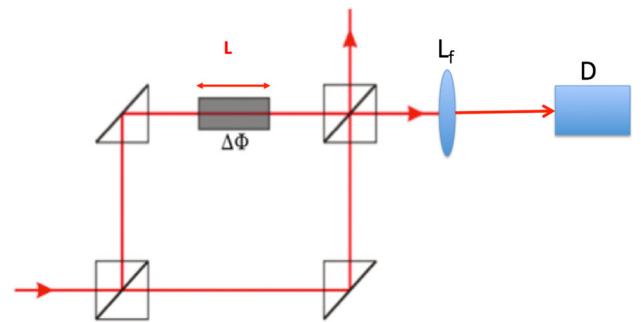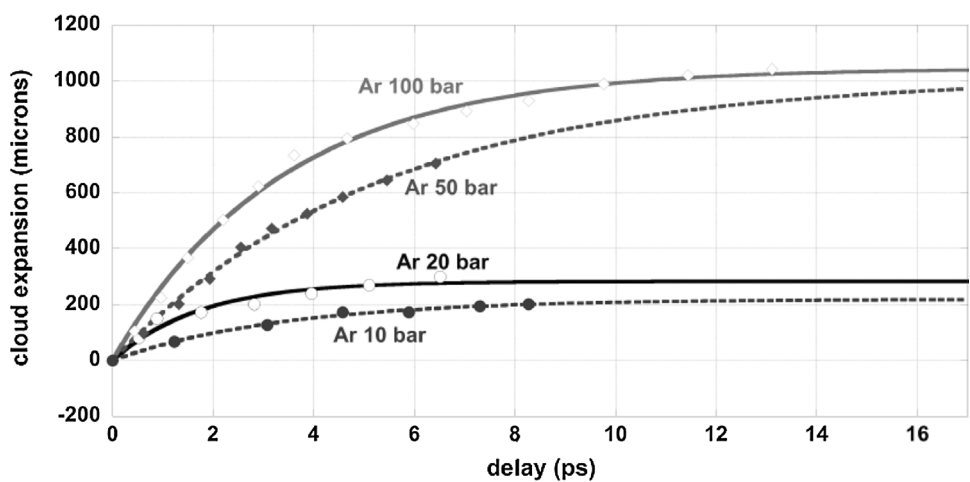
$$\langle n_e \rangle = \frac{1}{L} \int n_e \, dl$$

we see that

$$\frac{\Delta\Phi}{\pi} = \frac{L}{\lambda} \frac{\langle n_e \rangle}{n_{cr}} \tag{3}$$

or in other words, the fringe shift (phase shift in units of π) is proportional to the plasma length over the wavelength of the probing laser times the average density (defined over the line of sight) over the critical density.

In all practical situations, the last optical element in the Mach–Zender interferometer is slightly tilted in order to introduce fringes, i.e. a horizontal spatial carrier heterodyned frequency, with spatial wavelength λ_{het}. The carrier frequency is used to move the experimental information (i.e. the phase plane perturbation) away from the zero order in Fourier space, where all the low-frequency noise (such as spatial intensity fluctuations) is concentrated. In practice the presence of the fringes allows to more easily measure the phase displacement by simply observing the fringe shift.

The following figures show examples of interferometric images with laser-produced plasmas.

The first one (Fig. 12) represents a plasma created in air in the focal point of the focusing lens by a Nd:YAG laser with E $\approx$ 100 mJ, λ = 1.064 μm, $\tau \approx$ 40 ps [34]. The probing laser was a fraction of the main laser converted to second harmonic (532 nm) and sent across the plasma with a variable delay. Operating at two different laser waveleng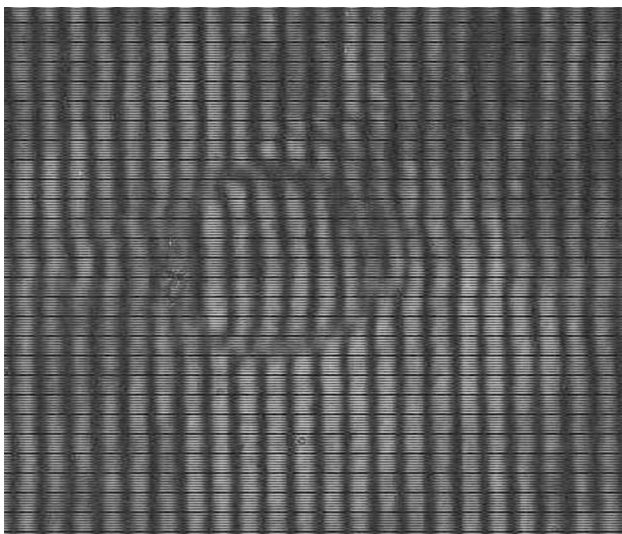ths is advantageous because it allows (for instance by using interference filters) to strongly reduce the noise coming from the scattered pump light to the image formed by the probe beam. In addition, choosing a probe beam with shorter wavelengths, allows probing higher plasmas densities.

The second image (Fig. 13) shows an interferogram of plasma obtained, with the same laser focused onto a solid target placed in vacuum. In this case the plasma expands without creating a shock wave (since there is no air around it to be compressed) and the density profile smoothly changes from the solid density down to the critical density and below. Let's notice that the typical atomic density of air is of the order of $\approx 10^{19}$ cm^{-3}, therefore all the created plasma is undercritical and transparent to the probe beam: we see the fringes everywhere. Instead in the case of plasma from solid target, there is an overcritical region where the fringes disappear.

For sake of completeness, we recall here that one common method to retrieve the phase shift from the interferogram is to use Fourier transformation. This method was introduced early in the history of laser produced plasma [35] and then improved by using fast Fourier transform (FFT) techniques [36]. This methodology works very well when interferograms are only marginally affected by noise and reduction of fringe visibility. In order to produce accurate phase-shift maps when low-quality images are dealt with, more recently procedures for phase-shift map computation using ridge extraction in the continuous wavelet transform (CWT) framework were introduced [37]. Comparative analysis of the accuracy performances of CWT and of FFT approaches have shown that CWT-
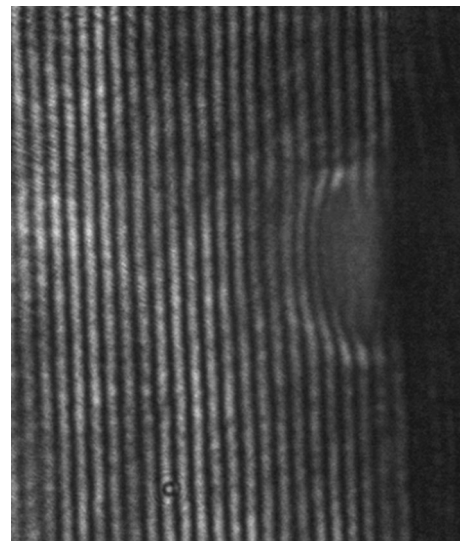

Fig. 12 Interferogram of a plasma created in air in the focus of the lens by a Nd:YAG laser with E $\approx$ 100 mJ, λ = 1.064 μm, $\tau \approx$ 40 ps [34]. The probe beam crosses the plasma 10 ns after the interaction of the pump beam has created the plasma. The size of the image is 200 × 170 μm

Fig. 13 Interferogram of a plasma expanding in vacuum created by focusing a ps-laser beam [34] onto an iron needle. The probe beam crosses the plasma 10 ns after the interaction of the pump beam. The size of the image is 300 × 360 μm

based tools can produce phase maps which are considerably less noisy and can better resolve local inhomogeneities.

These images immediately show some characteristics of the plasma (in particular the dimension). However, according to Eq. 3, the plasma density profile $n_e(x,y,z)$ is not directly obtained though interferometry but one can only obtain the average density over the line-of-sight $\langle n_e \rangle$. In order to get the detailed density profile, one needs to do additional assumptions.

Planar Quasi-Homogeneous Plasma

In some cases, one can assume that the plasma is quite uniform over the distance L. This is for instance the case of plasmas created on planar target by irradiation of a laser beam with a large focal spot (diameter $\approx$ L) smoother using PZP or KPP, which produces a top-hat distribution of intensity. In this case one can reasonably neglect the plasma edges with thickness d $\ll$ L. In addition, by limiting the observation time so that the expansion of the plasma is also $\ll$ L, one can reasonably neglect 2D effects and assume a 1D plasma expansion.

For instance, in the work in [1], the detector was a streak camera providing temporal resolution. Its slit was placed perpendicular to the target plane (i.e. parallel to the direction of plasma expansion) as shown in Fig. 14.
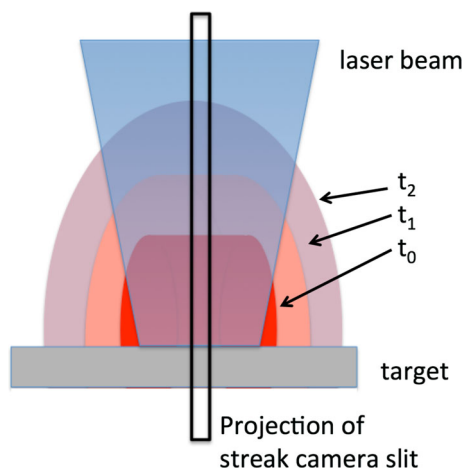
Fig. 14 Scheme of the experimental set-up used in [1]. The laser beam irradiates the solid target normally to the surface and the streak camera slit is perpendicular to the target surface and centered with respect to the focal spot. The laser beam was smoothed using Phase Zone Plate (PZP) thereby providing a top-hat irradiation profile and a "flat" plasma expansion (at least around the center of the focal spot and for short observation times). We schematically show the size of the plasma at different times t_0, t_1, t_2. Notice that at t_2 the plasma is bigger than the size of the laser focal spot and the expansion clearly becomes bidimensional even around the center of the focal spot
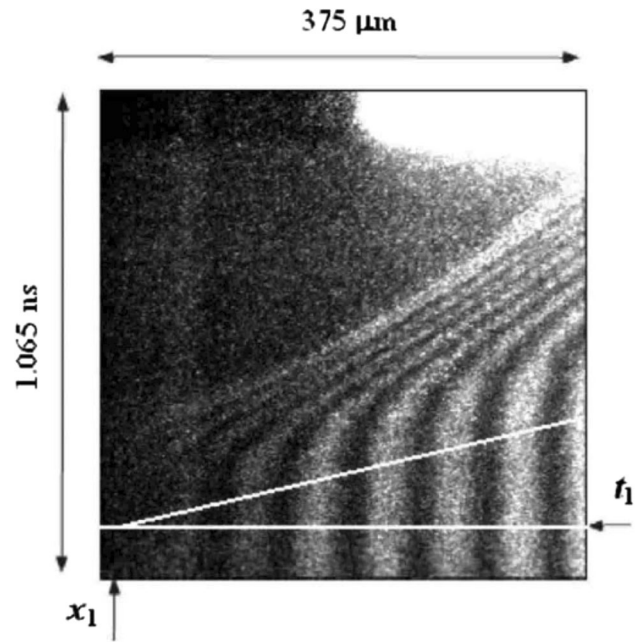
Fig. 15 Interferogram recorded with the streak camera on a planar CH_2 foil (shot at $E = 49.6$ J) Image size is 375 μm horizontal scale and 1.065 ns vertical scale. The vertical arrow shows the position x_1. The horizontal arrow roughly corresponds to the time t_1, at which the pump laser arrives on target. The white inclined line represents the ensemble of the points where the fringes begin to move (from [1])

Figure 15 shows a typical experimental result obtained using a Nd:YAG laser probe converted to 2ω with pulse duration longer than the desired observation window.

With all the assumptions, we have done, we can say that $n_e \approx \langle n_e \rangle$ and then we can simply apply Eq. 3 to retrieve electron density, which is here just a function of the distance from the planar foil and of time. Measuring the fringe shifts from Fig. 15 we get the plasma density profiles at different times, as shown in Fig. 16.
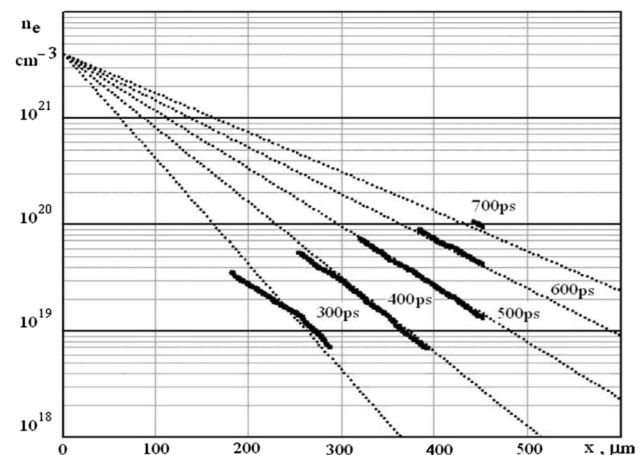
Fig. 16 Comparison of experimental profiles (obtained from the interferogram in Fig. 15) with the predictions of the analytic 1D model for a CH_2 target

The results in Fig. 16 show that in this case the density profiles agree quite well with the predictions of simple self-similar analytical models for isothermal plasma expansion, according to which

$$n_e(x,t) = n_{cr} \exp\left(-\frac{x - x_0}{c_s t}\right)$$

here c_s is the sound plasma velocity which is given in practical units by

$$c_s = 9.79 \times 10^5 \sqrt{\frac{\gamma Z^* T_e}{m}}$$

where c_s is in cm/s, T_e in eV, m is the average ion mass in the plasma in atomic units and γ is the adiabatic constant. Isothermal conditions are here provided by the fact that the laser pulse duration is comparable to the observation window (therefore the plasma is continuously heated by the laser) and by the large free path of thermal electrons in the plasma corona, assuring efficient energy exchanges and temperature uniformization.

The graphs in Fig. 16 allow inferring the plasma electronic temperature T_e. From Fig. 16 we also see that the accessible density range is between 7×10^{18} and 10^{20} cm^{-3}. Of course, low densities are hardly detectable because the induced phase shift is very low (the refraction index being very close to 1). As for high densities, although the critical density for the probe beam is $\approx 3.9 \times 10^{21}$ cm^{-3}, in reality light rays which travel through the higher density (higher refraction index) regions of the plasma are strongly deviated and will fall out the collection solid angle of the lens L_f (remind Fig. 11 and also see later the paragraph on shadowgraphy). Increasing the optical aperture (by using for instance larger diameter optics) this effect can be reduced but the disadvantage is that the spherical aberrations of the optical system are increased. In case a large aperture optical system is attempted, complex lenses such as doublets or triplets should be used for an acceptable spatial resolution of a few microns. However this remains an unavoidable problem in interferometry, implying that usually only densities up to a maximum of $\approx n_{cr}/10$ can be probed (we notice here that indeed the same limitation applies to shadowgraphy and schlieren)

Plasmas with Cylindrical Symmetry

In many cases one can assume that the plasma has an axial (cylindrical) symmetry. This is for instance the case of a laser beam (normally with axial symmetry) focused perpendicularly on the surface of a planar target, or the case of a plasma generated in a gas. In all these cases, the mathematical Abel transform allows getting the detailed profile
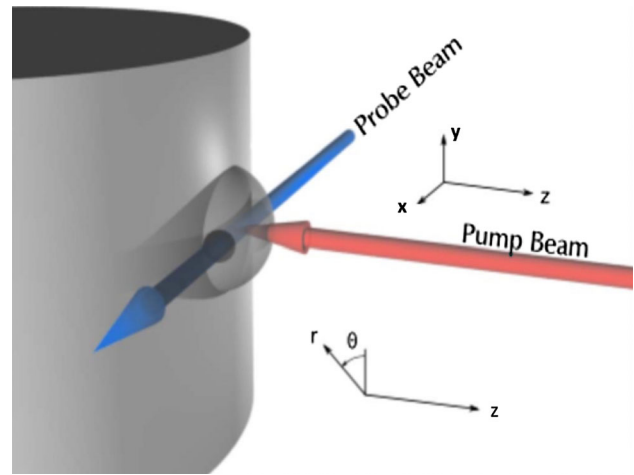

Fig. 17 Production ad probing of a plasma with cylindrical symmetry
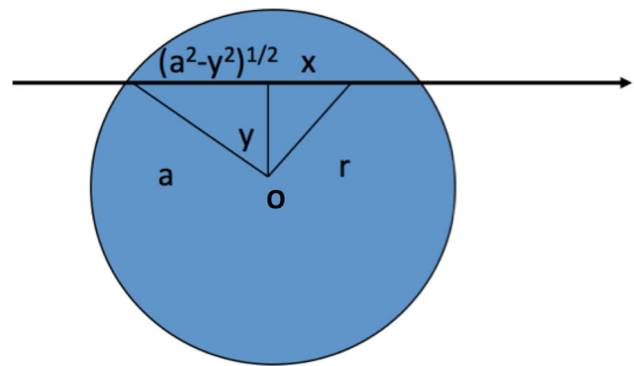

Fig. 18 Propagation of the probe laser beam inside the plasma of Fig. 16. Here a plane corresponding to a value of z has been selected. O is the center of symmetry, which also corresponds to the axis of the laser pump beam. The plasma radius is a

of electron density n_e as a function of spatial coordinates $n_e(r,z,t)$. See the experimental set-up schematically shown in Fig. 17 (notice again the use of needle as target)

Making a cut at level z, we have the situation described in Fig. 18.

Following the scheme in Fig. 18, the dephasing of the laser probe beam as it crosses the plasma at the position y, assuming as usual $n_e \ll n_{cr}$, is given by

$$\Delta\Phi(y) = \frac{k_0}{2n_{cr}} \int n_e dl = \frac{k_0}{2n_{cr}} \int_{-\sqrt{a^2-y^2}}^{\sqrt{a^2-y^2}} n_e(r) dx$$

Again this shows that dephasing depends on the areal plasma density (in units of electrons/m^2). If cylindrical symmetry does not exist, this quantity can still be calculated with relative good accuracy. When cylindrical symmetry exists the cubic density (electrons/m^3) can be extracted. By using the substitution

$$x = \sqrt{r^2 - x^2} \Rightarrow dx = -\frac{r\,dr}{\sqrt{r^2 - x^2}}$$

The dephasing $\Delta\Phi$ becomes

$$\Delta\Phi(y) = \frac{k_0}{2n_{cr}} \int n_e dl = \frac{k_0}{n_{cr}} \int_y^a \frac{n_e(r)}{\sqrt{r^2 - y^2}} dr$$

This is an integral equation of Volterra type, which has been studied by Abel. The dephasing function $\Delta\Phi(y)$ is the "Abel transform" of $n_e(r)$. If $n_e(a) = 0$, i.e. if the plasma has a finite size, one can invert it (Abel inversion) and get $n_e(r)$:

$$\frac{k_0}{n_{cr}} n_e(r) = \frac{1}{\pi} \int_r^a \frac{d}{dy}(\Delta\Phi(y)) \frac{dy}{\sqrt{y^2 - r^2}} dr$$

The "idea" behind Abel transform is shown in Fig. 19. One starts reconstructing the profile from the exterior (i.e. $y = a$), where one can assume that the value of density is uniform and the length of the (very short) plasma path is known. In this case $\Delta\Phi_1 = n_1 d_1$ and measuring $\Delta\Phi$ it is possible to deduce n_e. This information is then transported inside using the axial symmetry to the next path (next y value) where now it is possible to write $\Delta\Phi_2 = 2n_1d_2 + n_1 d_3$ and so on…

Let's notice that in reality from a mathematical point of view the Abel transform can be applied also when the condition $n_e(a) = 0$ is not satisfied. It is sufficient that $\Delta\Phi$ drops to zero quicker that $1/r$.

The Abel transform is a powerful tool but it also has severe drawbacks. First of all, we have seen (Fig. 19) that the information on the electron density is reconstructed staring form the exterior. This means that the errors at the plasma edge will reflect up to the center of the plasma, even very severely.

Second, the mathematical operation of Abel inversion is very sensitive to noise. Small fluctuations in the data ($\Delta\Phi$) can imply very large fluctuations in the retrieved electron d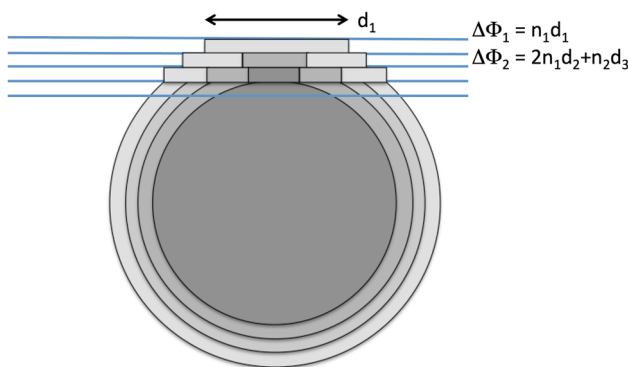ensity n_e. This implies that before performing the Abel inversion it is usually needed to filter the data in order to reduce noise, but this also imply a loss of information.

Third, the Abel inversion requires perfect symmetry while experimental results usually show some asymmetries. So, before applying the Abel transform one must find the most likely symmetry axis and then either average the two half-images or duplicate one of the two halves to obtain a full dephasing map (which either correspond to filtering and losing information or to introducing spurious data).

As an application of the case of plasmas with cylindrical symmetry and of Abel transform let's consider the experimental results presented in [38]. In this work a Ti:Sapphire laser with energy of 60 mJ, and a duration of 150 fs was split in two parts, one to be used as pump (40 mJ) and the other acting as probe (20 mJ). The pump pulse was focused by a single lens with $f = 100$ cm on the target to a peak intensity on target of 4×10^{15} W/cm^2. The probe beam was frequency doubled by a 2 mm thick BBO crystal. The probe beam was then injected in a Mach–Zender interferometer and the interferogram was imaged on a 12-bit CCD.

Aluminum wires with 200 μm diameter were used as target, again in order to eliminate the problem of tilting with respect to the probe direction. Moreover, since the focal spot size was much smaller than the wire radius, the interaction area could practically be considered as a planar one.

The delay line has been varied to introduce delays ranging from $t = 0$ ps to $\Delta t = 100$ ps by steps of 3 ps. In Fig. 20, four interferograms show the plasma expansion at different times. The image resolution was about 1.2 μm
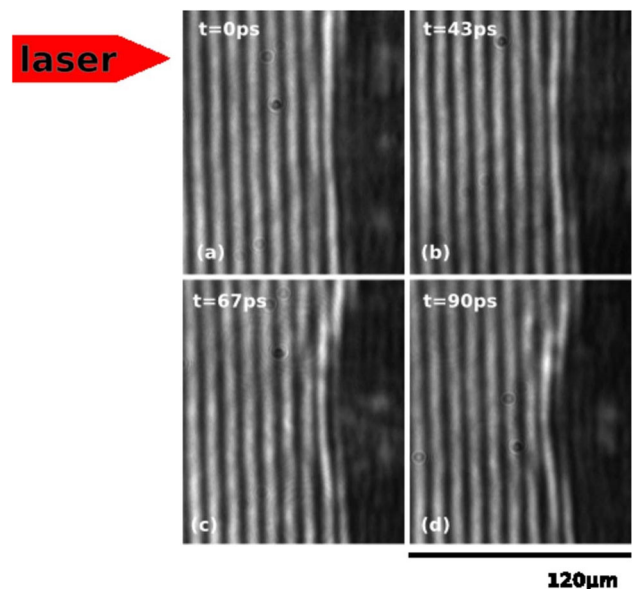
Fig. 19 Principle of Abel transform

Fig. 20 Interferograms showing plasma expansion at four different delays: a 0 ps, b 43 ps, c 67 ps, and d 90 ps (from [35])
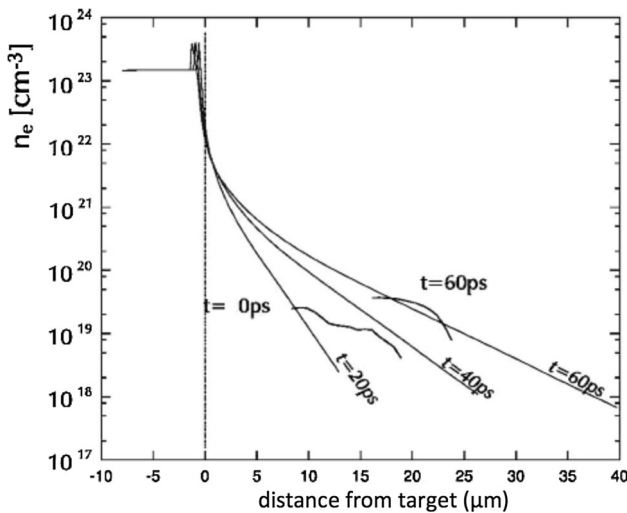
Fig. 21 Experimental plasma density profiles at 3 different delays: 0 ps, 20 ps, and 60 ps, and comparison with theoretical predictions (from [35])

given by diffraction limit and the interferometer interfringe was $\lambda_{het} \approx 10$ μm.

Some of the obtained density profiles are shown in Fig. 21 together with predictions from hydro simulations. Let's notice that unlike in the work previously presented (Ref. [1]), here the interferograms are recorder long after the end of the laser pulse (ps vs. fs) and hence the plasma expansion is rather adiabatic.

Polarimetry

The polarimetry diagnostic (Faraday rotation) was introduced in laser generated plasmas very early [4]. The application of the method for large density gradients dense plasmas accompanied by simultaneous shadowgraphy and interferometry is described in [39]. When a probe laser beam propagates in a magnetized plasma, the presence of the external magnetic field in the plasma create an anisotropy of the refractive index as [25, 40]:

$$n^2 = 1$$
$$+ X \left(1 - i\nu/\omega - \frac{Y_\perp^2}{2(1 - X - i\nu/\omega)} \pm \sqrt{\frac{Y_\perp^2}{4(1 - X - i\nu/\omega)}} \right)$$

where $X = n_e^2/n_{cr}^2$, $Y = \omega_{ce}/\omega$, $Y_\perp = Y\sin\theta$. Here θ is the angle between the direction of propagation of the probe beam $\vec{k}$ and the direction of the magnetic field and ω_{ce} is the electron cyclotron frequency. The polarimetry diagnostics uses this anisotropy to retrieve information on the magnetic field inside of the plasma.

The most commonly used approach to measure magnetic fields is through the Faraday rotation. This is the case

in which $\theta = 0$ and the polarization axis of the probe beam will change depending of the magnetic field strength and the plasma density. In the case of an underdense plasma with $X \ll 1$ and $Y \ll 1$, the analytical expression for the rotation of the polarization axis is

$$\Delta\Psi = \frac{1}{2} \int XY \cos\theta \frac{\omega}{c} dl \qquad (4)$$

Experimentally such rotation can be observed using a polarizing beam splitter like a Wollaston Cube, which allows the separation of the two components of polarization on an orthonormal basis $\overrightarrow{(e_x}, \overrightarrow{e_y)}$. The rotation of polarization is then the ratio of the two projections of the electric field on the basis $\overrightarrow{(e_x}, \overrightarrow{e_y)}$, i.e. it is $\Delta\Psi = \Psi_2 - \Psi_1 = E_{y2}/E_{x2} - E_{y1}/E_{x1}$. In the case of an external magnetic field of very high intensity, the rotation of polarization can become larger than $\pi/2$ defining the limits of this diagnostic. Generally, this diagnostic need to be used in combination with interferometry allowing to obtain the density profile, which, according to Eq. 4, is essential to retrieve the magnetic field map. This method to measure the magnetic field is well known and commonly used in astrophysics [41] or in the study of laser–plasma interactions [42]. When the magnetic field is purely orthogonal ($Y = Y_\perp$ or $Y_{II} = Y\cos\theta = 0$) Faraday rotation disappears.

When the magnetic field is not parallel to the direction of propagation of the probe beam, it is possible to use the Cotton–Mouton effect, which induces a modification of the ellipticity of the polarization during the propagation. In the case of an underdense plasma with $X \ll 1$ and $Y \ll 1$ this ellipticity modification is

$$\frac{b}{a} = \frac{1}{2} \int \frac{XY^2 \sin^2\theta}{1 - Y^2} \sin 2\beta \frac{\omega}{c} dl$$

where b/a is the ratio of the minor and major axis of the ellipse defining the polarization of the probe beam (i.e. $b/$
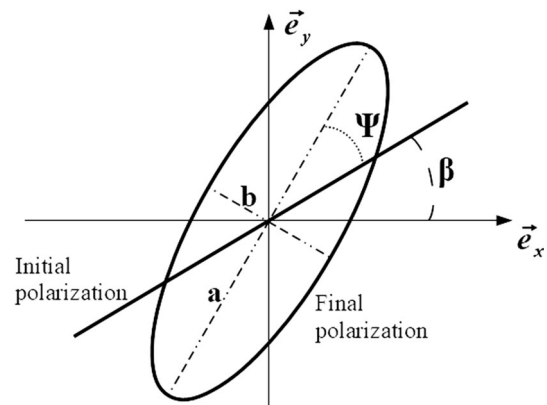

Fig. 22 The polarization ellipse and the polarization coordinate systems for a direction of propagation of the probe beam $\vec{k} = \vec{e_z}$

$a = 0$ for linear polarization beam and $b/a = 1$ for circular polarization) and β is the angle between the main polarization axis of the probe beam and $\vec{e_x}$, as described in Fig. 22.

If the magnetic field is only on the plane perpendicular to the direction of propagation of the probe beam, a simple polarizing cube can be used giving $b/a = E_y/E_x$ when the probe beam is initially linearly polarized along $\vec{e_x}$ (here E_y and E_x are the components of the electric field of the probe electromagnetic wave along $\vec{e_x}$ and $\vec{e_y}$. Caution needs to be used with this diagnostic method as the Cotton-Mouton effect is much weaker than the Faraday rotation.

If the magnetic field direction is unknown, one need to obtain the complete polarization of the laser as defined by the Stokes parameters [43]:

$$S = \begin{pmatrix} S_0 \\ S_1 \\ S_2 \\ S_3 \end{pmatrix} = \begin{pmatrix} E_x^2 + E_y^2 \\ E_x^2 - E_y^2 \\ E_a^2 - E_b^2 \\ E_r^2 - E_l^2 \end{pmatrix}$$

These parameters correspond to the projection of the laser intensity on 3 different basis $\overrightarrow{(e_x}, \overrightarrow{e_y)}$, $\overrightarrow{(e_a}, \overrightarrow{e_b)}$ oriented at 45° with respect to the previous one, and $\overrightarrow{(e_r}, \overrightarrow{e_l)}$, the basis indicating left-had and right-hand rotations. Using the Stokes vector, we can retrieve the angle defining the polarization of the probe beam as:

$$\Psi = \frac{1}{2} \arctan\left(\frac{S_2}{S_1}\right)$$

$$\arctan\frac{b}{a} = \frac{1}{2} \arctan\left(\frac{S_3}{\sqrt{S_1^2 + S_2^2}}\right)$$

The easiest way to measure this parameter is to use a polarimeter measuring the intensity on the different basis show previously (Fig. 23). The intensity on the basis
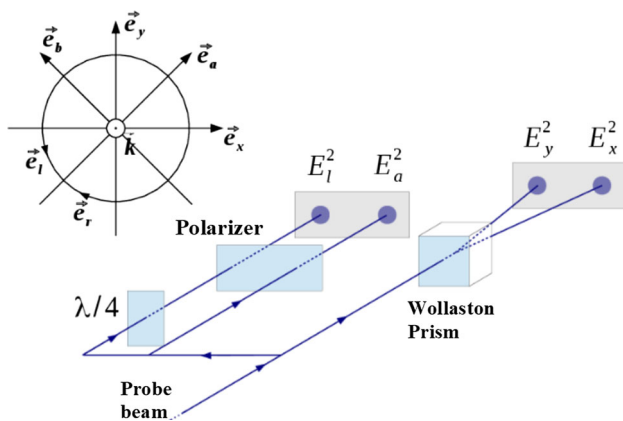

Fig. 23 Example of a two CCDs polarimeter. The three different basis $\overrightarrow{(e_x}, \overrightarrow{e_y)}$, $\overrightarrow{(e_a}, \overrightarrow{e_b)}$ and $\overrightarrow{(e_r}, \overrightarrow{e_l)}$, are represented on the top-left corner

$\overrightarrow{(e_x}, \overrightarrow{e_y)}$ is obtained using a polarizing beam splitter (i.e. a Wollaston in the figure). These two projections give the intensity S_0 of the probe beam. A polarizer at 45° extract the intensity on the direction $\vec{e_a}$, which allows calculating direction $\vec{e_b}$ as $E_b^2 = S_O - E_a^2$. Finally, the combination of a $\lambda/4$ wave plate and a polarimeter at 45° transmits only the intensity of the left-hand rotating component E_l wave (which allows calculating E_r as $E_r^2 = S_O - E_l^2$).

The Cotton–Mouton polarimetry method (measuring the Stokes parameters) was first introduced in high intensity laser solid target interaction experiments at CLF/RAL by Tatarakis et al. [44, 45]. More recently it has been successfully developed and applied by the research group at TIFR in India. They used a probe beam at normal incidence on the target and four different photodiodes measuring the 4 Stokes parameters with time resolution (but without spatial resolution) [46]. Later they improved the method using a CCD detector allowing obtaining spatially resolved images of the Stokes parameters in the magnetized plasma [47].

A limitation of the method is anyway that when the magnetic field is very strong, reaching MGauss intensities, Eq. 4 can no longer be used as the change of ellipticity becomes non-bijective. This means that different values of the magnetic field can produce the same final ellipticity.

In addition, as is the case of Faraday rotation, the polarimetry diagnostic does not allow alone to extract the magnetic field as the change of polarization also depends on the plasma density. Coupling to interferometry is therefore needed to estimate the magnetic field amplitude.

[For sake of completeness, we notice here that magnetic field in the high density region (near the critical density), which is not accessible with external probe pulses, can be estimated using self-generated harmonics in high intensity laser matter interactions. Tatarakis et al. [48] and Gopal et al. [49] measured the change of polarization produced by the Faraday effect on the self-generated harmonics of the laser allowing to get information about the magnetic field deeper inside the plasma, but without information about the path of the harmonics inside the plasma (i.e. the exact position of harmonics generation)].

As example of use of the polarimetry diagnostic, we refer to an experiment recently performed at the CELIA laboratory with the laser ECLIPSE, a Ti:Sapphire system delivering pulses of 30 fs and 200 mJ. These were focused on Al-coated SiO_2 targets to an intensity of 5×10^{17} W/cm^2 [47].

The laser beam was split in two part, one (95% of the energy) to be used as pump, and the other acting as the probe (2.5% of the energy). The pump pulse was focused by an off-axis parabola on the target at 45°. The probe beam was frequency doubled by a 1-mm thick BBO crystal

Fig. 24 Spatial mapping of the Stokes parameters of the reflected probe beam 1.5 ps after the interaction of the laser at 5×10^{17} W/cm^2 on an Al-coated fused silica target. **a** S_0, **b** $s_1 = S_1/S_0$, **c** $s_2 = S_2/S_0$, **d** $s_3 = S_3/S_0$
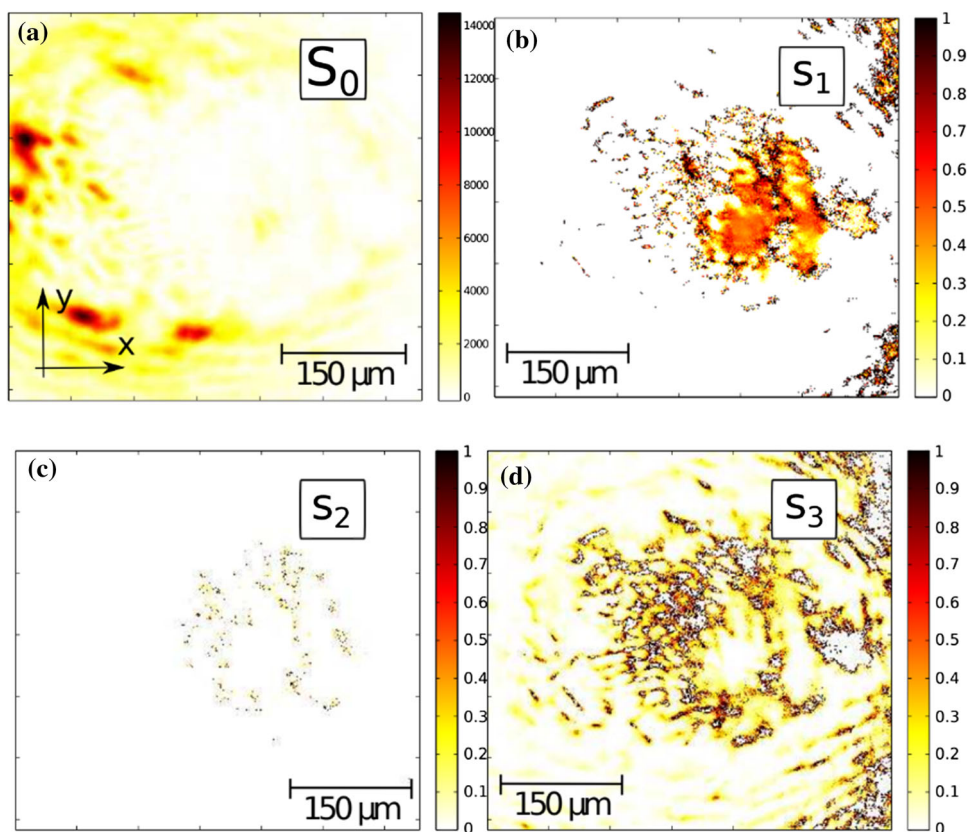

and focused at normal incidence by a lens with focal length f = 220 mm on a focal spot on target of about 300 μm. Frequency doubling was introduced with the dual purpose of letting the probe pulse propagate to higher density regions and of using a probe wavelength different from the pump, avoiding the problem introduced by the scattered pump light entering the interferometer beam path.

The probe beam was reflected by the plasma and collect by an imaging system (through the same lens used for focusing) with a 10 × magnification and then injected in the polarimeter which used two 12-bit charge coupled devices (CCD), each CCD measuring 2 of the 4 stokes parameters. The spatial resolution of the diagnostic was

10 μm. A delay line allowed introducing delays of the probe beam ranging from $\Delta t = -3$ ps to $\Delta t = 50$ ps in steps of 0.4 ps. Here Δt is the delay between the arrival on target of the main beam and of the probe beam (hence a negative Δt means that the probe beam arrives on target before the main pulse has struck it). The plasma density and scalelengths (which as explained before are needed to retrieve the value of magnetic field) were characterized suing interferometry in the same experiment.

Figure 24 shows the map of the four Stokes parameters, which are used to retrieve the ellipticity and rotation of the main polarization axis (Fig. 25). In this shot, we can observe that the rotation of the polarization axis is

Fig. 25 Spatial mapping of angles **a** $arctan(b/a)$, **b** Ψ
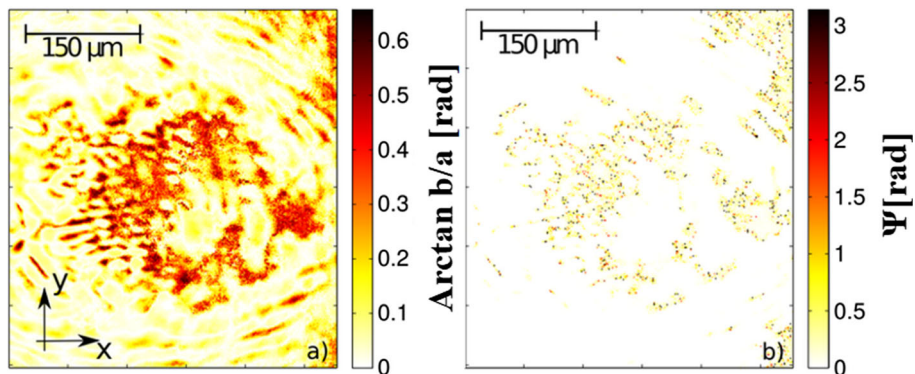
negligible while its ellipticity is changing drastically. This implies the presence inside the plasma of a strong azimuthal magnetic field.

Due to the fact that the magnetic field strength is very large, the relation between magnetic field and elicit change is no longer bijective, as discussed earlier. Hence it is difficult to estimate the absolute value of the magnetic field. However, the comparison with simulation results, allowed to infer a value ~ 10 MegaGauss.

The polarimetry diagnostic allows measuring the magnetic field inside an underdense plasma with good temporal resolution (equal to the duration of the probe laser pulse) and good spatial resolution (define by the resolution of the imaging system).

Conclusions

This paper was addressed to give a few examples of the large variety of diagnostics needed to study laser-produced plasmas. We have focused on optical diagnostics for the undercritical region of the plasma: shadowgraphy, schlieren, interferometry, polarimetry showing some of the challenges related to measuring the detailed characteristics of small-size, fast-varying plasmas.

References

1. A. Aliverdiev, D. Batani, R. Dezulian, T. Vinci, A. Benuzzi-Mounaix, M. Koenig, V. Malka, Coronal hydrodynamics of laser-produced plasmas by interferometry. Phys. Rev. E. **78**, 046404 (2008)
2. K.L. Lancaster, J. Pasley, J.S. Green, D. Batani, S. Baton, R.G. Evans, L. Gizzi, R. Heathcote, C. Hernandez Gomez, M. Koenig, P. Koester, A. Morace, I. Musgrave, P.A. Norreys, F. Perez, J. Waugh, N. Woolsey, Temperature profiles derived from transverse optical shadowgraphy in ultra-intense laser plasma interactions at 6×10^{20} W/cm^2. Phys. Plasmas **16**, 056707 (2009)
3. M. Manclossi, D. Batani, D. Piazza, S. Baton, F. Amiranoff, M. Koenig, H. Popescu, P. Audebert, J.J. Santos, E. Martinolli, M. Rabec Le Gloahec, A. Antonicci, C. Rousseaux, M. Borghesi, C. Cecchetti, V. Malka, T. Hall, Optical shadowgraphy and proton imaging as diagnostics tools for fast electron propagation in ultra-high-intensity laser-matter interaction. Radiat. Eff. Defects Solids **160**, 575 (2005)
4. J.A. Stamper, B.H. Ripin, Faraday-rotation measurements of megagauss magnetic fields in laser-produced plasmas. Phys. Rev. Lett. **34**, 138 (1975)
5. F. Rosmej, A. Faenov, T. Pikuz, F. Flora, P. Di Lazzaro, S. Bollanti, N. Lisi, T. Letardi, A. Reale, L. Palladino, D. Batani, S. Bossi, A. Bernardinello, A. Scafati, L. Reale, A. Zigler, M. Fraenkel, E. Cowan, Inner-shell satellite transitions in dense short pulse plasmas. J. Quant. Spectrosc. Radiat. Transf. **58**, 859 (1997)
6. E. Martinolli, M. Koenig, J.M. Boudenne, E. Perelli-Cippo, D. Batani, T.A. Hall, Conical crystal spectrograph for high brightness X-ray Kalpha spectroscopy in subpicosecond laser-solid interaction. Rev. Sci. Instrum. **75**, 2024 (2004)
7. H. Nishimura, Y. Inubushi, Y. Okano, S. Fujioka, T. Kai, T. Kawamura, D. Batani, A. Morace, R. Redaelli, C. Fourment, J. Santos, G. Malka, A. Boscheron, A. Casner, M. Koenig, T. Nakamura, T. Johzaki, H. Nagatomo, K. Mima, X-ray polarization spectroscopy to study energy transport in ultra-high intensity laser produced plasmas. J. Phys. **112**, 022080 (2008)
8. M. Koenig, J.M. Boudenne, P. Legriel, T. Grandpierre, D. Batani, S. Bossi, S. Nicolella, R. Benattar, A computer driven crystal spectrometer with CCD detectors for X-ray spectroscopy of laser–plasmas. Rev. Sci. Instrum. **68**, 2387 (1997)
9. A. Stepanov, A. Starostin, V. Roerich, V. Makhrov, A. Faenov, A. Magunov, T. Pikuz, I. Skobelelev, F. Flora, S. Bollanti, P. Di Lazzaro, N. Lisi, T. Letardi, L. Palladino, A. Reale, D. Batani, S. Bossi, A. Bernardinello, A. Scafati, L. Reale, A. Osterheld, W. Goldstein, Modelling of the He-like magnesium spectral line radiation from the plasma created by XeCl and Nd-glass lasers. J. Quant. Spectrosc. Radiat. Transf. **58**, 937 (1997)
10. D. Batani, F. Bianconi, A. Giulietti, D. Giulietti, L. Nocera, Second harmonic polarisation and conversion efficiency in laser produced sparks. Opt. Commun. **70**, 38 (1989)
11. A. Giulietti, D. Giulietti, D. Batani, V. Biancalana, L. Gizzi, L. Nocera, E. Schifano, Spectroscopic evidence for sum frequency of forward and backscattered light in laser plasmas. Phys. Rev. Lett. **63**, 524 (1989)
12. D. Giulietti, V. Biancalana, D. Batani, A. Giulietti, L. Gizzi, L. Nocera, E. Schifano, Three half harmonic generation in laser plasma interaction: evidence for plasmon propagation. Il Nuovo Cimento **13 D**, 845 (1991)
13. L. Antonelli, D. Batani, A. Patria, O. Ciricosta, C. Cecchetti, P. Koester, L. Labate, A. Giulietti, L.A. Gizzi, A. Moretti, M. Richetta, L. Giuffrida, L. Torrisi, M. Kozlova, J. Nejdl, M. Sawicka, D. Margarone, B. Rus, G. Schurtz, X. Ribeyre, M. Lafon, C. Spindloe, T. O'Dell, Laser-plasma coupling in the shock-ignition intensity regime. Acta Tec. **56**, T57 (2011)
14. F. Pisani, M. Koenig, D. Batani, T. Hall, D. Desenne, J. Bruneau, C. Reverdin, Toroidal crystal spectrometer for time-resolved X-ray absorption diagnostic in dense plasmas. Rev. Sci. Instrum. **70**, 3314 (1999)
15. T. Hall, J. Al-Kuzee, A. Benuzzi, M. Koenig, J. Krishnan, N. Grandjouan, D. Batani, S. Bossi, S. Nicolella, Experimental observation of the shift and width of the aluminum K absorption edge in laser shock compressed plasmas. Europhys. Lett. **41**(5), 495–500 (1998)
16. D. Batani, L. Antonelli, S. Atzeni, J. Badziak, F. Baffigi, T. Chodukowski, F. Consoli, G. Cristoforetti, R. de Angelis, R. Dudzak, G. Folpini, L. Giuffrida, L.A. Gizzi, Z. Kalinowska, P. Koester, E. Krousky, M. Krus, L. Labate, T. Levato, Y. Maheut, G. Malka, D. Margarone, A. Marocchino, J. Nejdl, P. Nicolai, T. O'Dell, T. Pisarczyk, O. Renner, Y.J. Rhee, X. Ribeyre, M. Richetta, M. Rosinski, M. Sawicka, A. Schiavi, J. Skala, M. Smid, C. Spindloe, J. Ullschmied, A. Velyhan, T. Vinci, Generation of high pressure shocks relevant to the shock-ignition intensity regime. Phys. Plasmas **21**, 032710 (2014)

17. A. Ravasio, M. Koenig, S. Le Pape, A. Benuzzi-Mounaix, H.S. Park, C. Cecchetti, P. Patel, A. Schiavi, N. Ozaki, A. Mackinnon, B. Loupias, D. Batani, T. Boehly, M. Borghesi, R. Dezulian, E. Henry, M. Notley, S. Bandyopadhyay, R. Clarke, T. Vinci, Hard X-ray radiography for density measurement in shock compressed matter. Phys. Plasmas **15**, 060701 (2008)

18. A. Ravasio, S. Le Pape, A. Benuzzi-Mounaix, L. Romagnani, C. Cecchetti, D. Batani, T. Boehly, M. Borghesi, R. Dezulian, L. Gremillet, E. Henry, D. Hicks, B. Loupias, A. McKinnon, N. Ozaki, H.S. Park, P. Patel, A. Schiavi, T. Vinci, R. Clarke, M. Notley, S. Bandyopadhyay, M. Koenig, Proton radiography of a shock compressed target. Phys. Rev. E. **82**, 016407 (2010)

19. M. Koenig, B. Faral, J.M. Boudenne, D. Batani, S. Bossi, A. Benuzzi, Use of optical smoothing techniques for shock wave generation in laser produced plasmas. Phys. Rev. E Rapid Commun. **50**, R3314–R3317 (1994)

20. A. Benuzzi, W. Nazarov, M. Koenig, J. Krishnan, B. Faral, M. Temporal, D. Batani, L. Muller, F. Torsiello, T. Hall, N. Grandjouan, Dynamics of laser produced shocks in foam-solid targets. Phys. Plasmas Lett. **5**, 2827–2829 (1998)

21. D. Batani, A. Benuzzi, M. Koenig, I. Krasyuk, P. Pashinin, A. Semenov, I. Lomonosov, V. Fortov, Problems of measurement of dense plasma heating in laser shock wave compression. Plasma Phys. Controll. Fusion **41**, 93–103 (1999)

22. S. Skupsky, S. Kacenjar, Measuring fuel ρR for inertial fusion experiments using neutron elastic-scattering reactions. J. Appl. Phys. **52**, 2608 (1981)

23. J.A. Frenje, D.T. Casey, C.K. Li, J.R. Rygg, F.H. Séguin, R.D. Petrasso, V. Yu Glebov, D.D. Meyerhofer, T.C. Sangster, S. Hatchett, S. Haan, C. Cerjan, O. Landen, M. Moran, P. Song, D.C. Wilson, R.J. Leeper, First measurements of the absolute neutron spectrum using the magnetic recoil spectrometer at OMEGA. Rev. Sci. Instrum. **79**, 10E502 (2008)

24. T. Caillaud, O. Landoas, M. Briat, S. Kime, B. Rossé, I. Thfoin, J.L. Bourgade, L. Disdier, V.Y. Glebov, F.J. Marshall, T.C. Sangster, Development of the large neutron imaging system for inertial confinement fusion experiments. Rev. Sci. Instrum. **83**, 033502 (2012)

25. I.H. Hutchinson, *Principles of Plasma Diagnostics* (Cambridge University Press, Cambridge, 1987)

26. S. Minardi et al., Opt. Lett. **33**, 86 (2008)

27. M.M. Michaelis et al., Opt. Laser Technol. **23**(5), 283 (1991)

28. M.M. Michaelis, O. Willi, Opt. Commun. **36**(2), 153 (1981)

29. G. de Izarra, C. De Izarra, Quantitative shadowgraphy made easy. Eur. J. Phys. **33**(6), 1821 (2012)

30. G.S. Settles, *Schlieren and Shadowgraph Techniques* (Springer, Berlin, 2001)

31. D. Haberberger, S. Ivancic, S.X. Hu, R. Boni, M. Barczys, R.S. Craxton, D.H. Froula, Measurements of electron density profiles using an angular filter refractometer. Phys. Plasmas **21**, 056304 (2014)

32. D. Batani, S.D. Baton, M. Manclossi, D. Piazza, M. Koenig, A. Benuzzi-Mounaix, H. Popescu, C. Rousseaux, M. Borghesi, C. Cecchetti, A. Schiavi, Laser-driven fast electron dynamics in gaseous media under the influence of large electric fields. Phys. Plasmas **16**, 033104 (2009)

33. D. Batani, S.D. Baton, M. Manclossi, J.J. Santos, F. Amiranoff, M. Koenig, E. Martinolli, A. Antonicci, C. Rousseaux, M. Rabec

Le Gloahec, T. Hall, V. Malka, T.E. Cowan, J. King, R. Freeman, Ultra-intense laser-produced fast electron propagation in gas jets. Phys. Rev. Lett. **94**, 055004 (2005)

34. A. Faenov, A. Magunov, T. Pikuz, D. Batani, G. Lucchini, F. Canova, M. Piselli, Bright, point X-ray source based on a commercial portable 40 ps Nd YAG laser system. Laser Part. Beams **22**, 373–379 (2004)

35. D.W. Sweeney, D.T. Attwood, L.W. Coleman, Interferometric probing of laser produced plasmas. Appl. Opt. **15**, 1126–1128 (1976)

36. K.A. Nugent, Interferogram analysis using an accurate fully automatic algorithm. Appl. Opt. **18**, 3101 (1985)

37. P. Tomassini, A. Giulietti, L.A. Gizzi, M. Galimberti, D. Giulietti, M. Borghesi, O. Willi, Analyzing laser plasma interferograms with a continuous wavelet transform ridge extraction technique. Appl. Opt. **40**(35), 6561 (2001)

38. A. Flacco, A. Guemnie-Tafo, R. Nuter, M. Veltcheva, D. Batani, E. Lefebvre, V. Malka, Characterization of a controlled plasma expansion in vacuum for laser driven ion acceleration. J. Appl. Phys. **104**, 103304 (2008)

39. M. Tatarakis et al., Phys. Plasmas **5**(3), 682 (1998)

40. C.B. Wharton, M.A. Heald, *Plasma Diagnostics with Microwaves* (Wiley, New York, 1965)

41. I.B. Zeldovich, A.A. Ruzmaikin, D.D. Sokolov, *The Fluid Mechanics of Astrophysics and Geophysics*, vol. 3 (Gordon and Breach Science Publishers, New York, 1983), p. 381

42. M. Borghesi, A.J. Mackinnon, R. Gaillard, O. Willi, A. Pukhov, J. Meyer-ter Vehn, Large quasistatic magnetic fields generated by a relativistically intense laser pulse propagating in a preionized plasma. Phys. Rev. Lett. **80**, 5137–5140 (1998)

43. S.E. Segre, A review of plasma polarimetry—theory and methods. Plasma Phys. Control. Fusion **41**(2), R57 (1999)

44. M. Tatarakis et al., Nature **415**, 280 (2002)

45. M. Tatarakis et al., Phys. Plasmas **9**(5), 2244 (2002)

46. A.S. Sandhu, A.K. Dharmadhikari, P.P. Rajeev, G.R. Kumar, S. Sengupta, A. Das, P.K. Kaw, Laser-generated ultrashort multi-megagauss magnetic pulses in plasmas. Phys. Rev. Lett. **89**, 225002 (2002)

47. S. Mondal, V. Narayanan, A.D. Lad, S. Ahmed, S. Sengupta, A. Das, Z.M. Sheng, P.K. Kaw, G. Ravindra Kumar, Measurement of hot electron transport in overdense plasma via self induced giant magnetic pulses. J. Phys. Conf. Ser. **44**, 022049 (2010)

48. M. Tatarakis, A. Gopal, I. Watts, F.N. Beg, A.E. Dangor, K. Krushelnick, U. Wagner, P.A. Norreys, E.L. Clark, M. Zepf, R.G. Evans, Measurements of ultrastrong magnetic fields during relativistic laser–plasma interactions. Phys. Plasmas **9**, 2244–2250 (2002)

49. A. Gopal, S. Minardi, M. Burza, G. Genoud, I. Tzianaki, A. Karmakar, P. Gibbon, M. Tatarakis, A. Persson, C.-G. Wahlström, Megagauss magnetic field generation by ultra-short pulses at relativistic intensities. Plasma Phys. Control. Fusion **55**, 035002 (2013)